Supplementary Materials

Cerium-Doped Ferroelectric $Hf_{0.5}Zr_{0.5}O_2$ Memristors for Low-Variability Multilevel Memory and Synaptic Plasticity

Xiaoxia Yu[1], Jiaqi Li[1], Jinhao Guan[1], Yumeng Bai[2], Jun Miao[1], Jinxia Deng[1], Lihong Li[2], Qiang Li[1], Kun Lin[1], Xianran Xing[1*]

[1] Institute of Solid State Chemistry, University of Science and Technology Beijing, Beijing 100083, China

[2]School of Materials Science and Engineering, University of Science and Technology Beijing, Beijing 100083, China.

***Corresponding author: xing@ustb.edu.cn**

Experimental Section

Preparation of HZO films

Undoped HZO/LSMO/STO heterostructures were fabricated on $SrTiO_3$ (STO) substrates following the same procedure used for the Ce-HZO films. Prior to deposition, the STO substrates were pre-annealed at 750 °C for 1 h in the PLD chamber. The laser fluence was 1 J cm^{-2}. A $La_{0.67}Sr_{0.33}Mn_{O3}$ (LSMO) bottom electrode layer was first deposited at 750 °C under an oxygen pressure of 20 Pa. The undoped HZO ceramic target was prepared by a conventional solid-state reaction using hafnium oxide powder (HfO_2, Bide Pharmatech, 99%) and zirconium oxide powder (ZrO_2, Macklin, 99%) with an Hf:Zr molar ratio of 1:1. The mixed powders were sintered at 1400 °C for 10 h to obtain the HZO ceramic target. The HZO thin films were deposited at 750 °C with a laser repetition rate of 2 Hz under an oxygen pressure of 20 Pa. After deposition, the samples were cooled to room temperature at a rate of 10 °C min^{-1} under an oxygen pressure of 5000 Pa. Pt top electrodes with a thickness of approximately 100 nm and a diameter of 50 μm were deposited at room temperature by magnetron sputtering through a shadow mask. The growth conditions were kept identical to those used for the Ce-HZO films.

Characterization of HZO Control Films

X-ray diffraction (XRD) measurements were carried out using a PW3040 X'Pert Pro diffractometer (PANalytical) with Cu Kα radiation. X-ray absorption spectroscopy (XAS) measurements were performed at the BL10B beamline of the National Synchrotron Radiation Laboratory, China. X-ray photoelectron spectroscopy (XPS) measurements were performed using the Thermo ESCALAB 250 spectrometer. Ferroelectric properties were characterized by polarization-voltage (P–V) measurements using an aixACCT TF-Analyser 2000 system at 1000 Hz over a voltage range from -5 to +5 V. Electrical measurements were performed using a Keithley 2611B source meter by applying bias to the Pt top electrode while grounding the LSMO bottom electrode.

SUPPLEMENTARY FIGURES

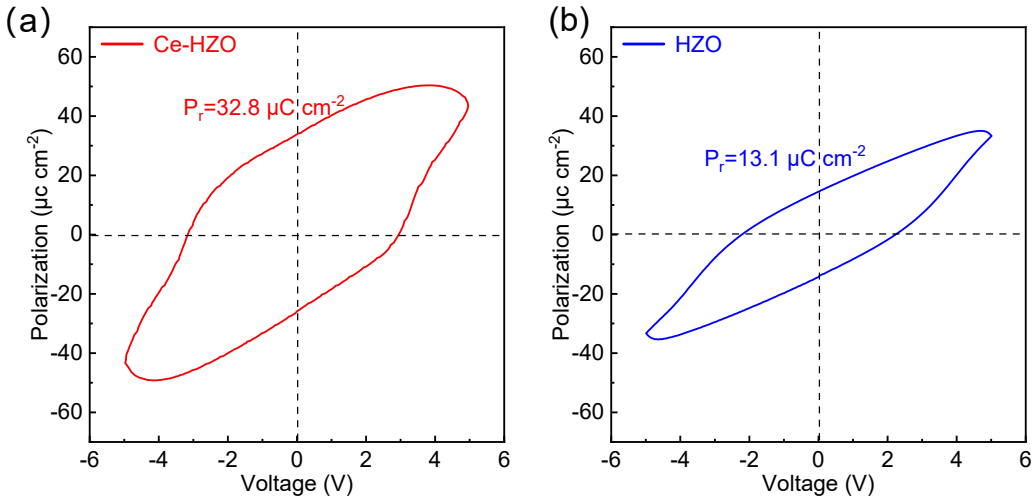

Fig. S1 Polarization–voltage (P–V) hysteresis loops of Ce-HZO and HZO thin films. (a) P–V hysteresis loop measured for the Ce-HZO film, showing an enhanced polarization with a maximum polarization value of ~32.8 μC cm^{-2}. (b) P–V hysteresis loop of the undoped HZO film measured under the same testing conditions, exhibiting a lower polarization value of ~13.1 μC cm^{-2}. The dashed lines indicate the zero-voltage and zero-polarization axes.

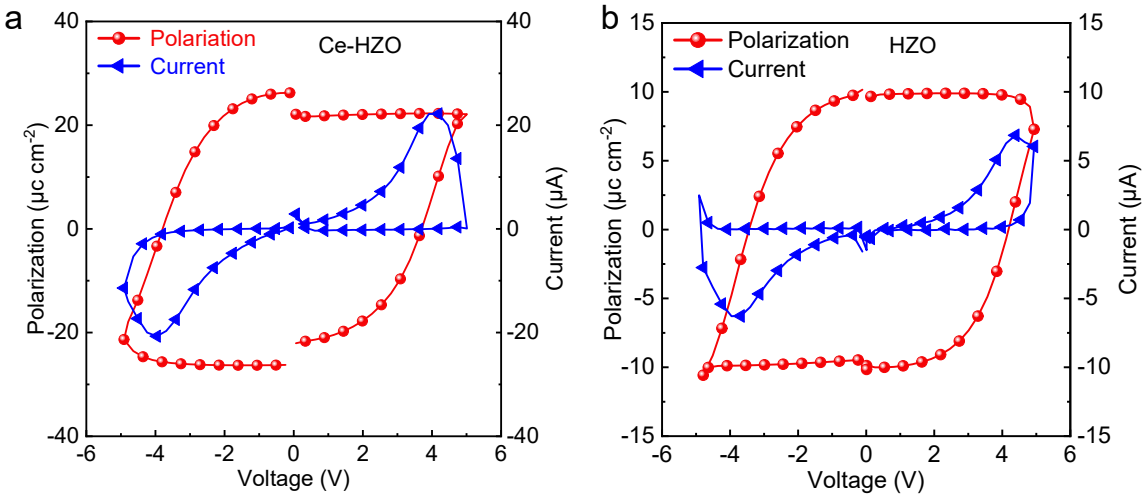

Fig. S2. Positive-Up-Negative-Down (PUND) characterization of switchable polarization in Ce-HZO and HZO thin films. (a) PUND polarization and transient current responses of the Ce-HZO film. (b) PUND polarization and transient current responses of the undoped HZO film measured under the same conditions. The red and blue curves represent the polarization and transient current responses, respectively. The PUND results confirm the presence of switchable polarization components after excluding non-switching contributions such as leakage current and capacitive charging.

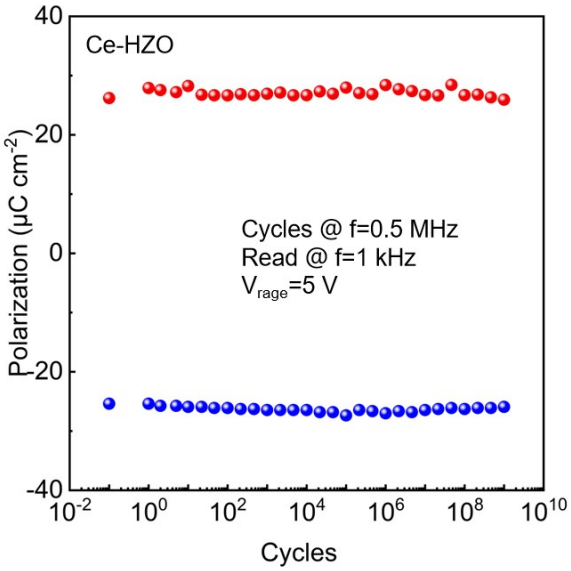

Fig. S3. Polarization cycling endurance of the Ce-HZO thin film.

Polarization endurance characteristics of the Ce-HZO thin film measured under bipolar cycling at f = 0.5 MHz with a voltage range of V_{range}= 5 V. The polarization values were read at f=1 kHz after selected cycling intervals. The positive and negative polarization states remain nearly stable over 10^9 electrical cycling, confirming the robust ferroelectric switching endurance of the Ce-HZO film.

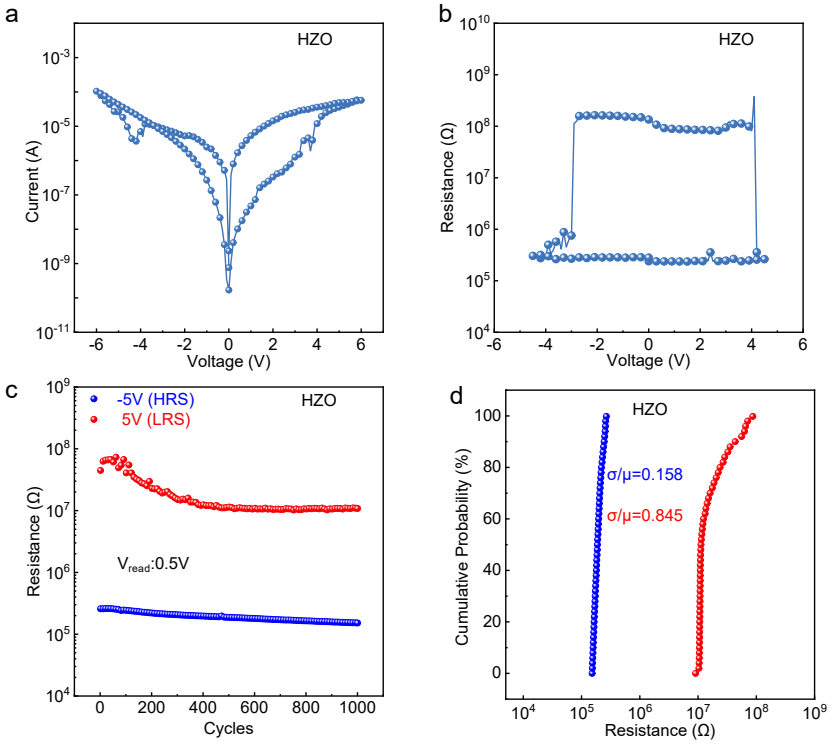

Fig. S4 Resistive switching characteristics of HZO memristors. (a) Representative bipolar I-V hysteresis curves measured from HZO. (b) Resistance hysteresis loops of HZO. (c) Cycle-to-cycle evolution of the high-resistance state (HRS) and low-resistance state (LRS) over 1000 cycles, read at V_{read} = 0.5 V. (d) Cumulative probability plots of the LRS and HRS resistances for the HZO devices.

As summarized in Fig. S4, the baseline resistive switching response and endurance statistics of the undoped HZO control device are presented. The bipolar I-V hysteresis and the corresponding program-read R-V loop confirm reversible switching between the high-resistance state (HRS) and low-resistance state (LRS) under the applied protocol. However, during endurance cycling, the HRS exhibits a noticeable downward drift from the initial 10^8 Ω level toward 10^7 Ω, whereas the LRS remains comparatively stable around 10^5 Ω. This asymmetric evolution is reflected in the cumulative probability distributions: the LRS distribution stays relatively narrow (σ/μ = 0.158), while the HRS distribution becomes significantly broader (σ/μ = 0.845). These results indicate that, for the undoped HZO device, cycle-to-cycle variability is dominated by the HRS instability, which reduces the effective state separation.

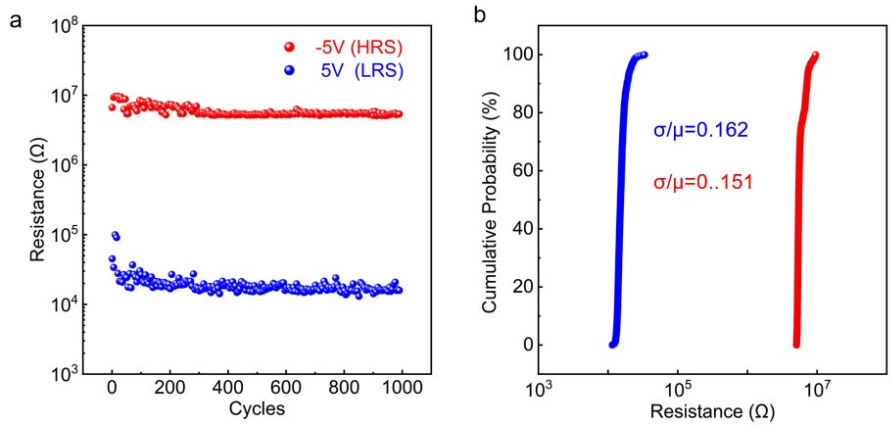

Fig. S5 Variability analysis of the 10 kPa oxygen-annealed Ce-HZO memristor. (a) Cycle-to-cycle evolution of the high-resistance state (HRS) and low-resistance state (LRS) over 1000 switching cycles after oxygen-pressure post-annealing. The HRS and LRS were programmed at -5 V and +5 V, respectively, and read at V_{read} = 0.5 V. (b) Cumulative probability distributions of the HRS and LRS resistance values extracted from the cycling data in (a). The calculated variability coefficients are σ/μ=0.151 for the HRS and σ/μ=0.162 for the LRS, indicating reduced cycle-to-cycle resistance dispersion after oxygen post-annealing.

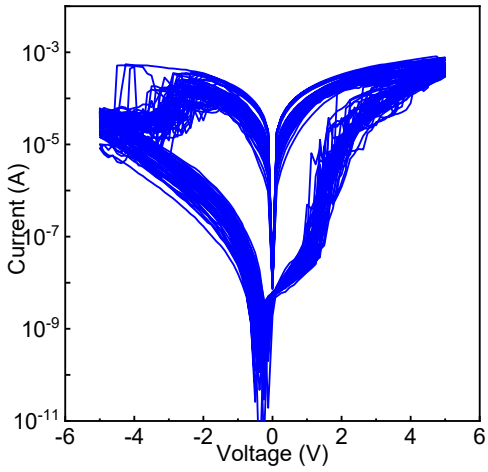

Fig. S6 The I−V curves obtained from 50 consecutive voltage sweeps.

As summarized in Fig. S6, the resistive switching repeatability of the Ce-HZO memristor was evaluated over 50 consecutive voltage sweeps (0 →+5 →-5 → 0 V). The overlaid I–V loops show consistent hysteresis across repeated cycles, indicating stable switching behavior and good cycle-to-cycle uniformity. The device switches toward a lower-resistance (higher-current) branch under positive bias and toward a higher-resistance (lower-current) branch under negative bias, confirming bidirectional resistance modulation that is required for synaptic weight increase and decrease in neuromorphic emulation.

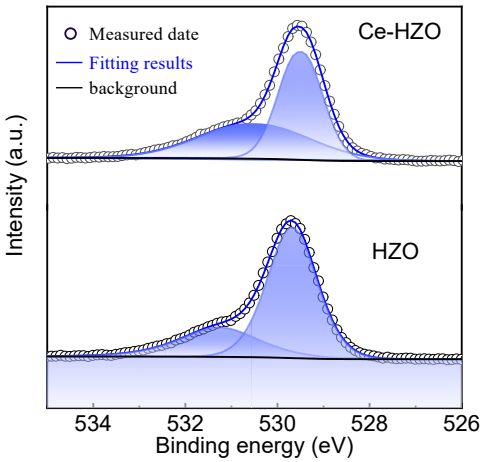

Fig. S7 O 1s spectra comparing Ce-HZO and HZO films.

Fig. S7 compares the O 1s core-level XPS spectra of the Ce-HZO and undoped HZO films (binding energies calibrated to the C 1s reference). Both spectra can be described by a dominant lattice-oxygen component centered near ~529 eV, together with a higher binding energy shoulder that is commonly fitted as a secondary O-related contribution. Relative to HZO, the Ce-HZO film shows a small shift of the main O 1s peak toward lower binding energy (from 529.61 to 529.47 eV). This concurrent negative shift in the O 1s line, together with the consistent core-level shifts observed for Hf and Zr in the main text, indicates a systematic change of the oxygen chemical environment upon Ce incorporation.

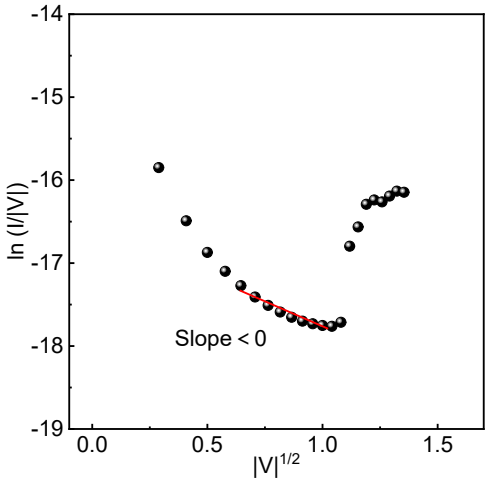

Fig. S8 The plot of ln(I/|V|)–$|V|^{1/2}$ for the HRS of the Ce-HZO film and the Poole-Frenkel fitting result.

Replot of the HRS I-V data as ln(I/|V|) versus $|V|^{1/2}$. The solid line is a linear fit performed in the 0-1.2 V window (low-field HRS). The fitted slope is negative, indicating that the PF representation does not yield the expected positive-slope linear behavior in this regime. Therefore, the low-field HRS conduction is not consistent with PF-dominated bulk trap emission.

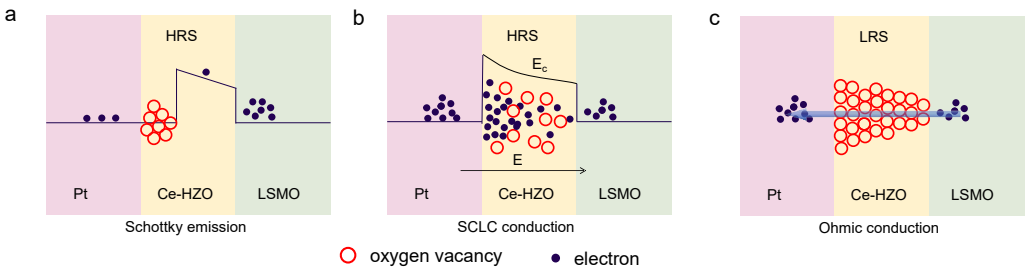

Fig. S9 Schematic diagrams of the conduction mechanism in Ce-HZO devices. (a) Low-field HRS (0–1.2 V), Schottky-type, interface-limited injection consistent with the linear lnI–$|V|^{1/2}$ relation in Fig. 4a. (b) HRS at higher fields: the intermediate-field regime (1.4–1.8 V) exhibits a Child's-law SCLC behavior ($I \propto V^2$) consistent with the log(I)–log(|V|) slope ≈ 2 in Fig. 4b, while the higher-field regime (2.0–5.0 V) shows a markedly increased exponent ($m \approx 5.02$), characteristic of trap-limited SCLC or a trap-filled-limit (TFL)-like behavior. (c) LRS (0–5 V), near-Ohmic transport consistent with the log(I)–log(|V|) slope ~ 1 in Fig. 4c, representing a low-resistance conductive configuration that weakens injection limitation. Red circles denote oxygen-vacancy-related defects (traps), and filled black dots denote electrons. The arrow indicates the effective electric-field direction under the defined polarity ($V_{Pt} > 0$).

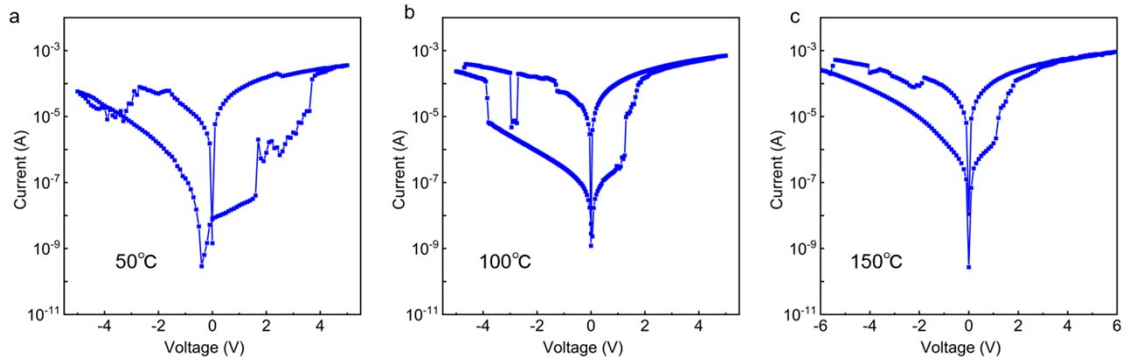

Fig. S10 Temperature-dependent I-V characteristics of the Ce-HZO memristor. (a-c) I-V curves measured at 50, 100, and 150 °C, respectively. The current is plotted on a logarithmic scale. With increasing temperature, the high-resistance branch exhibits a pronounced change, indicating the temperature-sensitive nature of the HRS transport. By contrast, the low-resistance branch remains comparatively stable and stays close to the 10^4 Ω level resistance state. This behavior is consistent with thermally activated interface-limited injection and trap-assisted transport in the HRS, while the LRS is governed by a more conductive near-ohmic transport configuration.

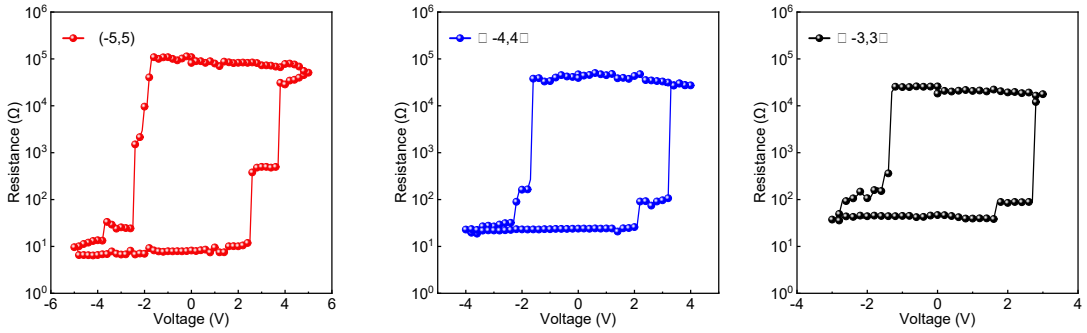

Fig. S11 Comparison of R-V values under different test conditions.

Fig. S11 compares the resistance-voltage (R-V) characteristics measured under different sweep boundaries, highlighting the protocol dependence of the programmed resistance states. When the full bipolar window (-5 to +5 V) is applied, the device exhibits the largest accessible resistance window and the most pronounced separation between the low- and high-resistance plateaus, indicating that the internal state can be driven across a wider range of configurations under the stronger programming field. Reducing the sweep boundary to (-4, +4 V) preserves the overall bipolar switching behavior but compresses the available resistance window, consistent with a smaller extent of state evolution during programming. Further limiting the sweep amplitude (-3, 3 V) results in a noticeably narrower R-V loop and weaker plateau separation, implying that the programming field is insufficient to fully access the high-resistance configuration and/or to complete the state transition within the same readout protocol.

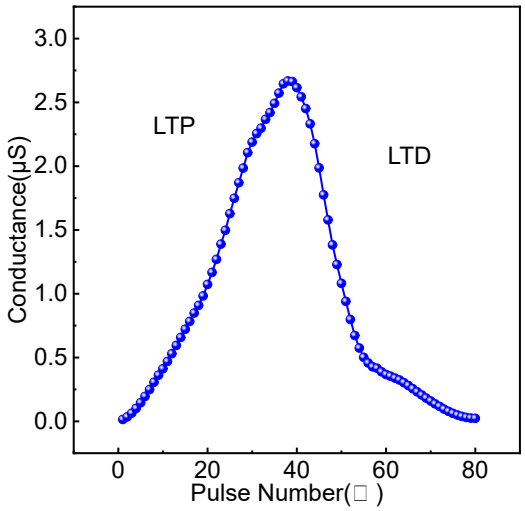

Fig. S12 Improved symmetry of LTP/LTD conductance updates by reducing the LTD pulse width.

LTP/LTD conductance-update characteristics of the Ce-HZO memristor measured under the optimized pulse condition of +2.5 V, 100 ms for potentiation and -2.2 V, 50 ms for depression. Compared with the original pulse condition of +2.8 V, 100 ms and -2.2 V, 100 ms, reducing the LTD pulse width slows down the early-stage conductance decay and produces a more gradual depression branch. The optimized device maintains a large dynamic range of $G_{max}/G_{min} \approx 1.87\times10^2$, while the global asymmetry factor decreases from $ANL_{avg} \approx 0.49$ to $ANL_{avg} \approx 0.27$. This result confirms that the pronounced asymmetry in the original LTP/LTD curve mainly originates from rapid conductance suppression during LTD and can be effectively mitigated by pulse-width engineering.

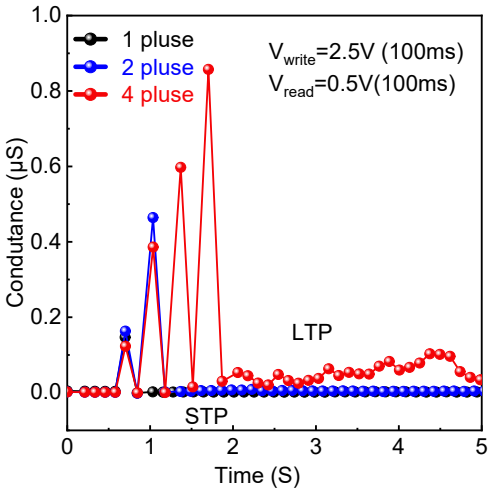

Fig. S13 Pulse number controlled transition from short-term plasticity (STP) to long-term potentiation (LTP) in Ce-HZO memristor.

The conductance dynamics in Fig. S13 reveal a pulse-number-controlled STP to LTP transition in our Ce-HZO memristor. 1-2 write pulses (V_{write}=2.5V, 100 ms) induce transient conductance enhancement (STP-like) that decays to baseline within seconds, whereas 4 pulses produce persistent potentiation (LTP-like) over the 5 seconds observation window. These observations are consistent with progressive accumulation of internal-state modification under repeated stimulation, rather than with an abrupt binary transition.

Table S1

Device	HRS σ/μ	LRS σ/μ	On/off ratio	Reference
Pt/Ce-HZO/LSMO	0.32	0.21	2×10^4	This work
Pt/Ce-HZO/LSMO (Annealing)	0.15	0.16	10^3	This work
Pt/HZO/LSMO	0.85	0.16	10^2	This work
Pt/LaTa-HZO/LSMO	0.38	3.83	10^4	Ref.1
Pt/HfO_2/TiO_x/Pt	0.43	0.48	5	Ref.2
TiN/HfO_2/CeO_x/TiN	0.37	0.48	10	Ref.3
Mg-doped HfO_x memristor	0.78	0.27	2.4×10^2	Ref.4
Mg-doped HfO_x memristor	0.28	0.15	5.7×10^2	Ref.4
Ti/HfO_x/Pt	0.47	0.46	10^2	Ref.5

Table S2

Pulse condition	+2.8 V, 100 ms; -2.2 V, 100 ms	+2.5 V, 100 ms; -2.2 V, 50 ms
G_{min} (S)	1.7686×10^{-5}	1.42804×10^{-5}
G_{max} (S)	3.68×10^{-3}	2.67×10^{-3}
Dynamic range, G_{max}/G_{min}	208.07	186.97
LTP linearity deviation	0.17	0.06
LTD linearity deviation	0.45	0.23
Global asymmetry factor, ANL_{avg}	0.49	0.27

Table S3

Parameter	Value
Fitting equation	$PPF(\Delta t) = A_1 \exp(-\Delta t / \tau_1) + A_2 \exp(-\Delta t / \tau_2)$
A_1	50
τ_1	0.08817
A_2	53
τ_2	0.59952
R^2	0.99257

Table S4

Timing window	Fitting equation	Amplitude	Time constant	R^2
Potentiation ($\Delta t > 0$)	$A_+ \exp(-\Delta t / \tau_+)$	A_+=34.71	τ_+ = 0.83	0.98
Depression ($\Delta t < 0$)	$-A_- \exp(\Delta t / \tau_-)$	A_-=54.35	τ_- = 0.64	0.96

References

1. H. W. Wang, J. P. Cao, W. Y. Deng, J. K. Wu, L. H. Yang, Z. J. Zhou, C. Feng, Y. Bai, Q. L. Li and J. Miao, Enhanced resistance switching ratio of Hf0.5Zr0.5O2-based film through reducing oxygen vacancy concentration, *Appl. Phys. Lett.*, 2025, **127**, 132901.
2. X. Ding, Y. Feng, P. Huang, L. Liu and J. Kang, Low-power resistive switching characteristic in HfO2/TiOx bi-layer resistive random-access memory, *Nanoscale Res. Lett*., 2019, **14**, 157.
3. G. Yao, Z. Qu, C. Li, Y. Peng, Q. Li, Z. Zeng, J. Dong, B. Zhang and M. P. Gashti, Improvement of the parameter distribution of TiN/HfO2/CeOx/TiN memristors by rapid thermal annealing, *J. Nanomater.*, 2022, **2022**, 6522007.
4. L.-H. Li, K.-H. Xue, L.-Q. Zou, J.-H. Yuan, H. Sun and X. Miao, Multilevel switching in Mg-doped HfOx memristor through the mutual-ion effect, *Appl. Phys. Lett.*, 2021, **119**, 153505.
5. Y. Song, X. Wang, Q. Wu, C. Wang, S. Du, L. Zhang and X. Miao, High switching uniformity in HfOx-based memristors by adding polydopamine-derived Ag nanoparticles on the electrode, *Appl. Phys. Lett.*, 2021, **118**, 223501.